Na–Ni–H phase formation at high pressures and high temperatures: hydrido complexes [NiH5]3– versus the perovskite NaNiH3

Kristina Spektor, Wilson A. Crichton, Stanislav Filippov, Johan Klarbring, Sergei I. Simak, Andreas Fischer, Ulrich Häussermann

Spektor, Kristina, Wilson A. Crichton, Stanislav Filippov, Johan Klarbring, Sergei I. Simak, Andreas Fischer, and Ulrich Häussermann. 2020. "Na–Ni–H phase formation at high pressures and high temperatures: hydrido complexes [NiH5]3– versus the perovskite NaNiH3." *ACS Omega* 5 (15): 8730–43. https://doi.org/10.1021/acsomega.0c00239.

ACS OMEGA

http://pubs.acs.org/journal/acsodf

Article

Na−Ni−H Phase Formation at High Pressures and High Temperatures: Hydrido Complexes $[NiH_5]^{3-}$ *Versus* the Perovskite $NaNiH_3$

Kristina Spektor,* Wilson A. Crichton, Stanislav Filippov, Johan Klarbring, Sergei I. Simak, Andreas Fischer, and Ulrich Häussermann*

Cite This: *ACS Omega* 2020, 5, 8730−8743

Read Online

ACCESS | Metrics & More | Article Recommendations | Supporting Information

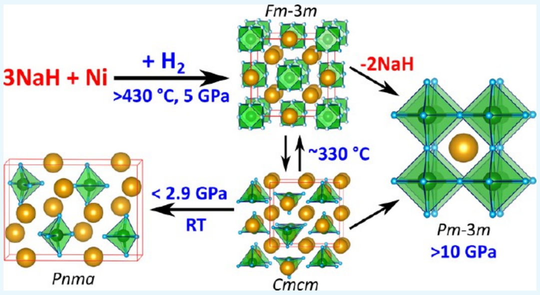

ABSTRACT: The Na−Ni−H system was investigated by *in situ* synchrotron diffraction studies of reaction mixtures NaH−Ni−H_2 at around 5, 10, and 12 GPa. The existence of ternary hydrogen-rich hydrides with compositions Na_3NiH_5 and $NaNiH_3$, where Ni attains the oxidation state II, is demonstrated. Upon heating at ∼5 GPa, face-centered cubic (*fcc*) Na_3NiH_5 forms above 430 °C. Upon cooling, it undergoes a rapid and reversible phase transition at 330 °C to an orthorhombic (*Cmcm*) form. Upon pressure release, Na_3NiH_5 further transforms into its recoverable *Pnma* form whose structure was elucidated from synchrotron powder diffraction data, aided by first-principles density functional theory (DFT) calculations. Na_3NiH_5 features previously unknown square pyramidal 18-electron complexes NiH_5^{3-}. In the high temperature *fcc* form, metal atoms are arranged as in the Heusler structure, and *ab initio* molecular dynamics simulations suggest that the complexes are dynamically disordered. The Heusler-type metal partial structure is essentially maintained in the low temperature *Cmcm* form, in which NiH_5^{3-} complexes are ordered. It is considerably rearranged in the low pressure *Pnma* form. Experiments at 10 GPa showed an initial formation of *fcc* Na_3NiH_5 followed by the addition of the perovskite hydride $NaNiH_3$, in which Ni(II) attains an octahedral environment by H atoms. $NaNiH_3$ is recoverable at ambient pressures and represents the sole product of 12 GPa experiments. DFT calculations show that the decomposition of Na_3NiH_5 = $NaNiH_3$ + 2 NaH is enthalpically favored at all pressures, suggesting that Na_3NiH_5 is metastable and its formation is kinetically favored. Ni−H bonding in metallic $NaNiH_3$ is considered covalent, as in electron precise Na_3NiH_5, but delocalized in the polyanion $[NiH_3]^-$.

■ INTRODUCTION

The finding of high temperature superconductivity in highly compressed H_2S[1] stimulated intensive research efforts into binary metal−H systems at high pressures, leading to the discovery of hydrogen-rich hydrides, also called superhydrides, under extreme pressure conditions.[2−5] Hydrogen-rich hydrides display a wide variety of unforeseen and previously unimaginable hydrogen structures, ranging from clathrate-like cages (e.g., LaH_{10}, CaH_6)[6−8] and oligomeric chain fragments (e.g., NaH_n)[9] to layer arrangements (e.g., FeH_5).[10] Characteristically, binary superhydrides are only stable at very high pressures in the Mbar range (70−150 GPa) and cannot be retained at ambient pressure. In contrast, ternary compounds may be retained and might even form under low(er) pressure conditions. Recently, it has been shown that already the application of modest pressures of around 5 GPa can afford new complex transition metal hydrides (CTMHs) in which group five and six metals attain unusually high coordination numbers in homoleptic complex ions such as $[CrH_7]^{5-}$ and $[NbH_9]^{4-}$.[11−13] Here, we demonstrate the accessibility of ternary hydrogen-rich hydrides in the Na−Ni−H system by using pressures up to 12 GPa and elevated temperatures up to 520 °C.

With the exception of Pd, late transition metals combine with elemental hydrogen only under high pressure conditions. The hydrogenation of Ni to γ-NiH requires about 1 GPa.[14−16] A higher hydride, monoclinic Ni_2H_3, has been recently synthesized at 60 GPa.[17] Both NiH and Ni_2H_3 cannot be quenched to ambient conditions. The situation changes radically when Ni is combined with an alkaline earth or rare earth metal. For example, the Ni-rich intermetallic compound $LaNi_5$ absorbs readily hydrogen into interstitial positions with varying occupancies ($LaNi_5H_{6.5}$), and Mg_2Ni is easily hydrogenated to yield the CTMH Mg_2NiH_4 featuring tetrahedral $[NiH_4]^{4-}$ complexes.[18,19] The nature of Ni−H interactions in

Received: January 17, 2020
Accepted: March 19, 2020
Published: April 8, 2020

the metallic interstitial hydride $LaNi_5H_{6.5}$ and the semiconducting CTMH Mg_2NiH_4 is rather different. There is even a third class of Ni hydride compounds, namely, perovskites (i.e., $CaNiH_3$).[20] Similar to CTMHs, Ni−H bonding in perovskites is covalent but delocalized over a polyanionic framework.[21,22]

In contrast with its heavier congeners Pd and Pt, Ni does not appear to combine easily with alkali metals in ternary hydrides. There is only one known representative, recently reported $LiNiH_3$ with the perovskite structure, which has been obtained by high pressure synthesis at 3 GPa.[23] Further, known hydrido complexes are restricted to tetrahedral $[NiH_4]^{4-}$ with formally zero-valent Ni.[24] Again, this is different to Pd and Pt, for which oxidation states of II (d^8) and even IV (d^6) are known in CTMHs with square planar and octahedral hydrido complexes, respectively.[24,25] We will show that with pressure, the Na−Ni−H system affords not only d^8-Ni hydrido complexes but also perovskite $NaNiH_3$.

■ EXPERIMENTAL METHODS

***In Situ* Powder X-ray Diffraction Studies at High Pressures.** The samples for the high pressure experiments were prepared in a glove box under an argon atmosphere because of air and moisture sensitivity of the starting materials. Powdered NaH (Sigma Aldrich, 90%) and powdered Ni metal (Sigma Aldrich, ≥99.9% trace metals basis) were carefully mixed at a molar ratio of 2:1 (NaH/Ni) and compressed into pellets. For the experiments at 5 and 10 GPa, sample pellets had an outer diameter (OD) of 2 mm and 1.5 mm height, while for the 12 GPa studies, dimensions were reduced to 1.4 and 0.75 mm, respectively. Ammonia borane (BH_3NH_3, Sigma-Aldrich, 97%) was used as hydrogen source. BH_3NH_3 has a well-defined decomposition behavior at high pressures and produces chemically inert BN as residual.[26] The amount of BH_3NH_3 used for each sample provided approx. 2.5 times molar excess of H_2 during the experiment with respect to nickel. NaH/Ni sample pellets were sandwiched between pelletized BH_3NH_3 and sealed inside NaCl capsules. The salt capsules employed at 5 and 10 GPa pressures had 3.0 mm OD and 3.8 mm height, while those used for 12 GPa runs were 2.4 mm OD and 2.8 mm height.

High pressure experiments at 5 and 10 GPa employed 14/8 multianvil assemblies. A detailed description of the 14/8 setup is provided elsewhere.[27] For reaching pressures above 12 GPa, the assembly was changed to a 10/5 type. Here, the sample capsules, protected by 2.8 mm OD BN sleeves, were inserted into 10 mm edge length Cr-doped MgO octahedra, along with two 2.8 mm OD ZrO_2 plugs and a nickel foil furnace (2.9 mm OD). Circular windows (2 mm OD) were cut in the Ni furnace along the beam direction to prevent the overlap with diffraction from the sample. Amorphous SiBCN rods (2 mm OD) and MgO rectangles (5 mm wide) were used as X-ray windows in the octahedra and gaskets, respectively, along the beam direction. Filled MgO octahedra were positioned between eight truncated tungsten carbide cubes (25 mm, Hawedia, ha7 grade) with 5 mm truncation edge length fitted with pyrophyllite gaskets. Both 14/8 and 10/5 assemblies were compressed at a rate of 1 bar/min oil pressure (∼2.5 and ∼3.2 GPa/h, respectively) to the target pressures and heated in the Voggenreiter-built modified-cubic press at beamline ID06-LVP, ESRF.[28] The heating was performed at various rates, ranging from 18 °C/min (comparatively fast) at $T < 400$ °C to <4 °C/min (comparatively slow) at higher temperatures or whenever a phase transition was expected. The heating was arrested each time the release of hydrogen from BH_3NH_3 was expected or the growth of ternary Na−Ni−H materials was detected. Pressure was estimated *in situ* from powder X-ray diffraction (PXRD) patterns using the equation of state (EOS) of NaCl, as reported by Birch.[29] For the 5 GPa experiments, temperature was evaluated from a D-type thermocouple calibration obtained in an independent run. The effect of pressure on the thermocouple EMF at 5 GPa is expected to be negligible.[30] During 10 and 12 GPa studies, the temperature was evaluated using the NaCl EOS.[29] Isobaric conditions were assumed during the heating, and the pressure was corrected after each >30 min dwell at constant power. Note that for the whole p, T range of the experiments, the Ni metal remained well below its melting curve.[31,32]

Angle-dispersive PXRD patterns were collected continuously at a constant wavelength, selected by the Si (111) double-crystal monochromator from the emission of a U18 cryoundulator at ∼6 mm magnetic gap. For 5 and 10 GPa runs, the wavelength (λ) was 0.22542 Å (2.15−10.7° 2θ range) and for the 12 GPa experiment, $\lambda = 0.2296$ Å. At 12 GPa, data were collected in 1.66−10.18° and 2.86−11.34° 2θ intervals at different stages of the experiment. A Detection Technology X-Scan series 1 linear pixilated detector was used for data acquisition. A diffraction data set was typically saved every 32 s during compression and decompression and every 3.2 s during heating. This data set consists of 32 × 0.1 s sequential exposures, which were subsequently 32× rebinned. Sample-to-detector distance and detector offset were calibrated using LaB_6-SRM660a (NIST). The *in situ* data were integrated, visualized, and manipulated using Fit2D software.[33] The 2θ angular positions of the diffraction peaks for the Na−Ni−H compounds and NaCl as a function of time were extracted from the compiled *in situ* data via the multiple fitting (MFIT) function in Fit2D.[34] Unit cell dimensions and volumes were extracted from the MFIT results by the least squares method. Indexing of powder patterns was done using the DICVOL algorithm within the CRYSFIRE package.[35]

Products from the high pressure experiments were recovered in a glove box under an argon atmosphere. Approximately half of the product from each run was sealed inside a glass capillary for *ex situ* characterization by PXRD.

***Ex Situ* PXRD Analysis.** PXRD patterns of recovered samples were collected at the beamlines ID15B and ID22 at the ESRF, Grenoble. The measurements at ID15B were performed at a constant wavelength of 0.41127 Å with the beam focused on a sample to 30 × 30 μm size and using a Mar555 flat-panel detector. The integration of 2D data was performed using Fit2D software.[36] High resolution synchrotron PXRD data were collected at ID22 using monochromatic radiation selected by a Si(111) crystal ($\lambda = 0.40008$ Å for the 5 GPa product and $\lambda = 0.3544$ Å for the 12 GPa product). Data acquisition was typically performed over a 0.5−32.9° 2θ range (0.002° step size) with the dedicated multianalyzer stage operating nine detectors in parallel, each preceded by a Si(111) analyzer crystal.

Le Bail analysis[37] and Rietveld refinement[38] of *in situ* and *ex situ* PXRD data were performed using Jana2006 software.[39] Before analyzing the patterns, they were corrected for background by subtracting the minimal value of observed intensity from the entire I_{obs} column. For the data collected at ID22, the peak shape was fitted with a pure Lorentzian profile, while the rest of the refinements were performed using pseudo-

Voigt peak profile function. In addition, ID22 data were thinned prior to the refinement so that only every second data point was used. *In situ* PXRD data were prepared for refinements by averaging 10−30 datapoints collected during the temperature dwell, which improved the signal-to-noise ratio and decreased possible contributions of texture to the refinement.

EOS Calculations. The calculation of the EOS for the $NaNiH_3$ perovskite was based on the *in situ* PXRD data collected on decompression during the 12 GPa experiment. The pressures were estimated from the cell volumes of NaCl using EOS, as reported by Birch.[29] The extracted data set of $NaNiH_3$ cell volumes as a function of pressure was introduced into EOSFit 5.2 software.[40] Data quality did not justify the use of the third order BM EOS model, and second order Birch−Murnaghan (BM) EOS was used instead. In addition, EOSfit 5.2 was employed to extract the EOS from the density functional theory (DFT) calculated p, V data. To make the resulting constants comparable with the fit of experimental data, a second order BM EOS model was used for the datasets obtained from DFT.

Theoretical Calculations. DFT enthalpy calculations were performed using the Vienna Ab Initio Simulation Package (VASP)[41,42] in the framework of the projector augmented wave method[43,44] within generalized gradient approximation and employing the Perdew−Burke−Ernzerhof parametrization of the exchange−correlation functional.[45,46] The cutoff energy for the plane wave basis set was 500 eV for all simulations. Structural relaxations employed a 3 × 4 × 5 Monkhorst−Pack (MP)[47] k-point grid for *Pnma* Na_3NiH_5 ($Z = 4$), a 4 × 4 × 4 grid for *Cmcm* Na_3NiH_5 ($Z = 4$) and Na_2NiH_4 (Na_2PtH_4 structure, $Z = 2$), a 14 × 14 × 14 grid for the perovskites $ANiH_3$ (A = Li, Na, K), and 1 × 1 × 1 (Γ-point) for $Z = 32$ Na_3NiH_5 supercells. Relaxations were performed with total energies converged better than 10^{-4} eV. Total energy calculations were carried out using the tetrahedron method with Blöchl correction[48] on a 4 × 4 × 4 MP k-point grid for *Pnma* and *Cmcm* Na_3NiH_5 and Na_2NiH_4, on a 14 × 14 × 14 grid for the perovskites $ANiH_3$, and on a 2 × 2 × 2 grid for $Z = 32$ Na_3NiH_5 supercells. For formation enthalpy calculations, total energy calculations were performed for NaH and Ni on 8 × 8 × 8 and 12 × 12 × 12 k-point grids, respectively. Molecular H_2 was considered with a pressure-independent enthalpy equal to −6.78 eV/molecule, as obtained from a total energy minimization of the H_2 molecule in a 10 × 10 × 10 $Å^3$ box.

Electronic density of states (DOS) calculations used spheres around the atomic sites (parameter RWIGS in VASP) with radii Na = 1.4, Ni = 0.8, and H = 1.1 Å. Bader analysis of the charge densities[49] was performed according to refs 50 and 51. The phonon dispersions and the phonon partial DOS were calculated on 2 × 2 × 2 supercells using the small displacement method,[52,53] as implemented in PhonoPy.[54] Total energies were converged better than 10^{-8} eV, referring to a 1 × 1 × 1 Γ-only (Na_3NiH_5) and a 8 × 8 × 8 k-point grid ($NaNiH_3$). The ionic positions were relaxed before the phonon calculations. The T_c estimation was performed using the Quantum Espresso code[55,56] and the Allen−Dynes-modified McMillan equation.[57] The cutoff energy for the plane waves was set to 60 Ry. The self-consistent calculations were performed on a 32 × 32 × 32 k-point grid. The electron−phonon coupling calculation was performed on a 4 × 4 × 4 k-point grid and using 0.1 as the value for the Coulomb pseudopotential μ^*.

Ab initio molecular dynamics (MD) simulations of cubic Na_3NiH_5 in the *NVT* ensemble (i.e., maintaining the number of atoms N, volume of the system V, and temperature T) were performed using the Nosé−Hoover thermostat at 1000 K and the experimental volume at ∼5 GPa and 510 °C (a = 7.19 Å). The simulation was done on a 2 × 2 × 2 supercell (Z = 32, 288 atoms) of the cubic unit cell of the HT-HP Na_3NiH_5 phase. The Brillouin zone integration was done at the Γ-point.

RESULTS AND DISCUSSION

Formation of Na_3NiH_5 at 5 GPa and Its Recovery to Ambient Pressure. Throughout this study, reaction mixtures $NaH/Ni/BH_3NH_3$ 2:1:∼0.8 were employed which corresponded to a Ni/H_2 ratio 1:∼2.5. In total, three experiments were performed at pressures around 5 GPa. All experiments showed good reproducibility of observations. In the following, we describe an experiment, compiled in Figure 1, during which slow heating/cooling rates and prolonged annealing steps were applied, and diffraction data were acquired for structural analysis.

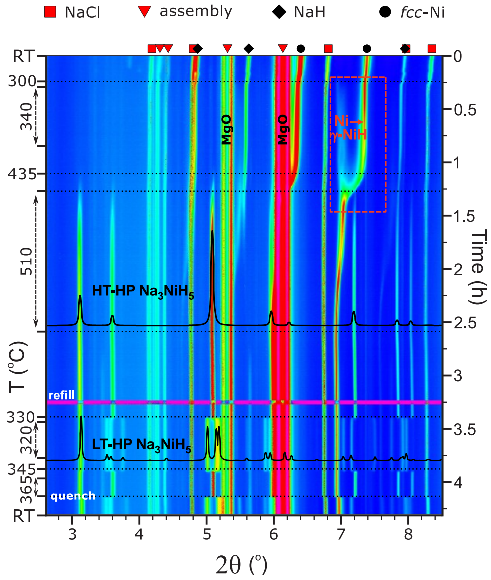

Figure 1. Compilation of *in situ* PXRD patterns (λ = 0.22542 Å) showing the formation and polymorphic behavior of Na_3NiH_5 at ∼5 GPa. Diffraction peaks arising from the 14/8 multianvil assembly (MgO, h-BN, $MgCr_2O_4$) are marked with red triangles.

The sample was compressed to ∼5.4 GPa and then heated to ∼340 °C. At these p, T conditions, BH_3NH_3 is expected to be completely decomposed into BN and hydrogen fluid.[26] The sample was then kept at 340 °C for about 30 min in order to equilibrate the system in the presence of hydrogen fluid. Before the initial heating was finished, formation of γ-NiH ($NiH_{\sim1}$) was noted at ∼300 °C as a set of diffuse peaks that appeared near the Ni metal reflections at lower 2θ angles. This is shown in the inset of Figure 1. In γ-NiH, the arrangement of metal atoms of face-centered cubic (*fcc*) Ni is retained, while H atoms are introduced in the octahedral voids of the metal structure, resulting in an expansion of the unit cell parameter.[14] Upon further heating, at approx. 435 °C, a new set of reflections emerged in the PXRD patterns. The d-spacings of these reflections could not be matched to any known compound, and their presence was interpreted as formation of a ternary high pressure, high temperature phase, in the following denoted HT-HP Na_3NiH_5. These new diffraction lines became more pronounced, and their intensities increased further when dwelling at 510 °C for 80 min (Figure 1). The diffraction peaks from HT-HP Na_3NiH_5 were indexed to a *fcc* lattice, with $a \approx 7.19$ Å at 510 °C.

After the dwell, the sample was slowly cooled at a rate of ~5 °C/min. At about 330 °C, a new set of intense diffraction peaks replaced those of the HT-HP Na_3NiH_5 phase, indicating a transformation to a low temperature polymorph (LT-HP Na_3NiH_5). The transition completed almost instantly (within 60 s). The LT-HP phase was indexed to a *C*-centered orthorhombic lattice (extinction symbol *C*-*c*-) with the unit cell parameters $a \approx 7.34$ Å, $b \approx 6.88$ Å, and $c \approx 7.22$ Å at 320 °C. The sample was dwelled for about 20 min and then slowly (3.5 °C/min) heated again to check the reversibility of the observed phase transition. The back-transformation of LT-HP Na_3NiH_5 to the HT-HP phase occurred at ~345 °C. Again, the transition proceeded instantaneously. After the transformation, the sample was dwelled at ~365 °C for 10 min and then quenched to room temperature. The HT-HP phase was not preserved by rapid cooling but was replaced with LT-HP Na_3NiH_5. The pressure was estimated as ~4.4 GPa after the temperature quench.

Figure 2a shows the unit cell parameters of both phases as a function of temperature and time as extracted from the *in situ* PXRD data. In addition, changes in the cell volumes are shown in Figure 2b. The average standard deviations for the cell parameters and unit cell volumes are within ±0.0052 Å (±0.461 Å^3) and ±0.0013 Å (±0.117 Å^3) for the HT-HP and LT-HP phases, respectively. The close numerical range of their cell parameters and volumes suggests that the two phases are polymorphs and that the orthorhombic lattice results from a distortion of the HT cubic cell on cooling. The splitting of the 220 reflection of the cubic HT phase during the transition to orthorhombic is shown in Figure S1. The volume change at the cubic to orthorhombic transition is approx. −2.1 Å^3 (0.57%). The rapid character of the transformation and rather small temperature hysteresis are indicative of a first order displacive phase transition.

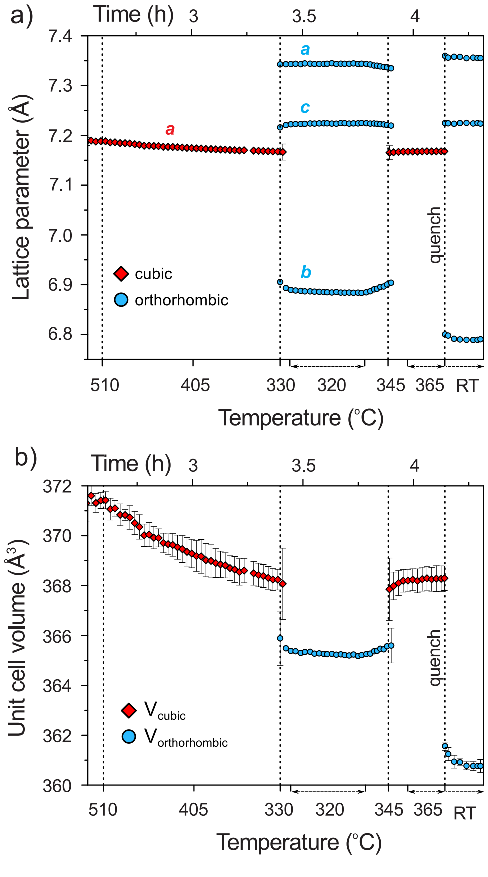

Figure 2. Cell parameters (a) and volumes (b) of cubic HT-HP and orthorhombic LT-HP Na_3NiH_5 as a function of temperature at ~5 GPa. Errors corresponding to the symbol size or smaller are not shown.

To conclude the experiment, the sample was decompressed to ambient conditions. At ~2.9 GPa, new diffraction peaks emerged. At ~2.6 GPa, the intensities of the new peaks increased, while the diffraction peaks of LT-HP Na_3NiH_5 became noticeably weaker, suggesting transformation to a different, low pressure, phase (LP Na_3NiH_5, see Supporting Information, Figure S2). At 1.4 GPa, the diffraction peaks of LT-HP Na_3NiH_5 were completely replaced. On final decompression, no significant further changes were observed, except for γ-NiH reverting back to *fcc* Ni. The sample was recovered at ambient conditions and used for *ex situ* PXRD examination. LP Na_3NiH_5 displayed a dark gray color, and when stored under Ar at room temperature, it decomposed over a period of several months.

Elucidating the Composition and Crystal Structures of Polymorphic Na_3NiH_5. For structural analysis of HT-HP and LT-HP Na_3NiH_5, PXRD data were prepared by averaging 20−40 patterns collected during the temperature dwell at 365 °C (cubic phase) as well as during the dwell at 320 °C and after the quench (orthorhombic phase). The HT-HP phase was analyzed using Le Bail fits to the space group $Fm\bar{3}m$ (225), whereas for the LT-HP phase space group *Cmcm* (63) was used. The *a* parameter for the cubic phase at 365 °C was refined to ≈7.169 Å. The cell parameters of the orthorhombic LT-HP phase at 320 °C were determined as $a \approx 7.344$ Å, $b \approx 6.883$ Å, and $c \approx 7.225$ Å. Possible metal atom arrangements were then identified using the Superflip algorithm on the extracted intensities within the Jana2006 package.[58] For the HP-HT phase, an antifluorite arrangement of the metal atoms was suggested, with Ni and Na occupying 4*a* and 8*c* Wyckoff sites, respectively. However, this solution could not be fitted reasonably to the experimental data using Rietveld refinement (see Supporting Information for details). The fit improved significantly when an additional atom partially occupied the 4*b* site, resulting in a Heusler arrangement of metal atoms. However, the type of atoms at this site was ambiguous: the Rietveld fit was equally good if 4*b* was occupied by ~0.3 Ni or ~0.7 Na atoms, yielding metal atom compositions $Na_2Ni_{\sim1.3}$ and $Na_{\sim2.7}Ni$, respectively. An analogous result was obtained for the orthorhombic LT-HP phase (*Cmcm*): Na and Ni atoms were found to occupy 4*c* and 8*e* sites, respectively, with one more atom partially occupying a second 4*c* site. The resulting compositions for the LT-HP phase reproduced those of the cubic polymorph. The simulated patterns for both cubic and orthorhombic phases with a metal atom composition $Na_2Ni_{\sim1.3}$ are overlaid in the *in situ* PXRD data in Figure 1 (*cf.* Figure S2 in the Supporting Information).

Further structural investigations then targeted the product LP Na_3NiH_5 recovered at ambient conditions. The structure determination and refinement were performed using integrated

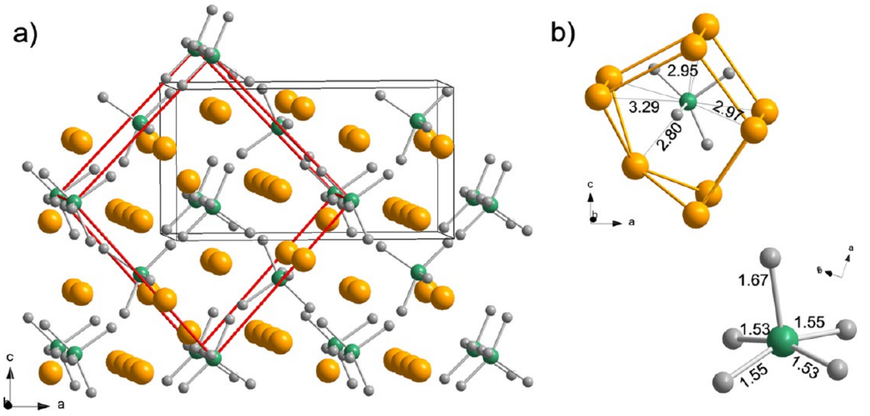

Figure 3. (a) *Pnma* structure of LP Na_3NiH_5 according to DFT optimization. Na, Ni, and H atoms are depicted as golden, green, and gray spheres, respectively. The arrangement of Ni atoms corresponds closely to a *fcc* structure (red unit cell). Na atoms are located in the vicinity of tetrahedral and octahedral voids. (b) Local coordination of a NiH_5^{3-} complex by 9 Na cations (top) and structure of a NiH_5^{3-} complex (bottom). Interatomic Na−Ni and Ni−H distances as obtained from DFT calculations are indicated (in angstroms).

2-dimensional PXRD data (*cf.* Supporting Information, Figure S3). Apart from leftover Ni metal and NaH, a set of reflections was present in the pattern, which could not be assigned to any known compound. The best indexing result suggested an orthorhombic unit cell with a *Pn-a* extinction symbol and approximate cell parameters $a \approx 10.41$ Å, $b \approx 7.37$ Å, and $c \approx 5.43$ Å. Le Bail analysis was initially carried out within the *P*222 (16) space group. A subsequent space group test then suggested *Pnma* (62). Structure solution resulted in a metal arrangement with 3Na:1Ni stoichiometry (Ni on a Wyckoff site 4*c*, and Na on sites 4*c* and 8*d*) and atomic coordinates very similar to K and N atoms in *Pnma* K_3NO_4 (potassium orthonitrate),[59] see Supporting Information for details. The obtained structure was used for Rietveld refinement against the experimental data and fitted well to the observed diffraction pattern ($R_{obs} \approx 7.7\%$, see also Supporting Information for refinement procedure), which strongly indicated the correctness of the metal composition and metal atom arrangement in LP Na_3NiH_5. Consequently, the Na_3Ni stoichiometry was also assumed for the HP forms. A Na_3Ni metal composition suggested 5 H atoms and Ni in an oxidation state II (d^8) or less likely 4 and 3 H atoms with Ni in the oxidation state I (d^9) and 0 (d^{10}), respectively.

In order to explore possible hydrogen atom arrangements, a simulated annealing (SA) global optimization algorithm in Endeavour 1.7 software was employed.[60] The previously refined "Na_3Ni" unit cell containing 12 Na^+ and 4 Ni^{2+} cations was introduced as a base to which either 16 or 20 H^- atoms (4 or 5 H^- per f.u.) were added. A simple repulsion potential for the charged ions was used during the optimization, while the positions of metal cations were kept fixed. The minimal Ni−H and Na−H distances were constrained to 1.5 and 2.0 Å, respectively. Several SA global optimization runs with 50−100 seeds were performed, which produced a range of "Na_3NiH_4" and "Na_3NiH_5" structures with various H^- ligand arrangements. These structures were then subjected to DFT optimization and their stability was assessed by the formation energy with respect to NaH, Ni, and H_2. As expected, formation energies of Na_3NiH_4 structures were clearly unfavorable against Na_3NiH_5 ones. Most of the stable Na_3NiH_5 configurations returned unprecedented square pyramidal NiH_5^{3-} complexes, which is shared by the geometry of the d^8-Co(I)H_5^{4-} complex in Mg_2CoH_5.[61]

The most stable Na_3NiH_5 configuration found by DFT optimization is shown in Figure 3, and its parameters are compiled in Table 1. The structure can be interpreted as a cubic close packing of NiH_5^{3-} complexes with all tetrahedral and octahedral interstices filled by Na^+ ions (Figure 3a). The distribution of Ni atoms follows the *fcc* metric; however, the location of cations deviates substantially from the ideal centers of interstices (i.e., 4*b* and 8*c* in $Fm\bar{3}m$). The local coordination and geometry of a NiH_5^{3-} complex is shown in Figure 3b. In the NiH_5^{3-} complex, the four basal ligands have similar and short distances to Ni (1.53 × 2, 1.55 × 2 Å), whereas the bond to the apical ligand is rather elongated (1.67 Å).

Table 1. DFT Optimized Ambient Pressure Structure of LP Na_3NiH_5 (Space Group: *Pnma* (62); *a* = 10.2566 Å, *b* = 7.3388 Å, and *c* = 5.5697 Å)

atom	site	*x*	*y*	*z*
Ni	4*c*	0.8848	0.25	0.7670
Na1	8*d*	0.1562	0.0179	0.8467
Na2	4*c*	0.0580	0.25	0.3793
H1	4*c*	−0.0076	0.25	−0.0381
H2	4*c*	0.8251	0.25	0.5118
H3	8*d*	0.0947	−0.0447	0.2632
H4	4*c*	0.7512	0.25	−0.0607

The optimized DFT structure of *Pnma* LP Na_3NiH_5 was then used as a model for a final Rietveld refinement against the experimental pattern. The hydrogen atom positions were kept unchanged during the refinement, and their U_{iso} parameters were fixed at 0.038 Å^2 (B_{iso} = 3 Å^2). The refinement procedure is described in Supporting Information. The refinement details and obtained crystal structure parameters are included in Tables 3 and 4, and the final Rietveld fit is shown in Figure 4. A simulated PXRD pattern of *Pnma* LP Na_3NiH_5 is overlaid in the compilation of *in situ* PXRD patterns collected during decompression (Figure S2).

Following the results of the LP Na_3NiH_5 structure solution, the elucidation of the HT-HP and LT-HP structures was revisited using Na_3NiH_5 stoichiometry. For a more detailed analysis of the HT-HP phase, a 2 × 2 × 2 supercell (*Z* = 32) of the *fcc* Heusler arrangement of Na and Ni atoms was assembled and 5 H atoms were placed around each Ni atom. This was then used as the initial structure for *NVT ab initio*

Table 2. DFT-Optimized Structure of LT-HP Na_3NiH_5 at 5 GPa (Space Group: *Cmcm* (63); a = 7.24484 Å, b = 6.63230 Å, and c = 7.22221 Å)

atom	site	x	y	z
Ni	4c	0	0.24955	0.25
Na1	8e	0.21107	0	0
Na2	4c	0	0.67043	0.25
H1	8f	0	0.69735	0.5453
H2	8g	0.2075	0.27691	0.25
H3	8c	0	0.00196	0.25

MD simulations using the experimental volume at ∼5 GPa and 510 °C (a = 7.19 Å). The simulation temperature was 1000 K. The system equilibrated after 1 ps, as indicated in the almost zero hydrostatic stress attained after this time (see Supporting Information, Figure S4), and NiH_5^{3-} complexes were found to perform reorientational dynamics (Figure S5). Accordingly, the *fcc* HT-HP Na_3NiH_5 structure can be considered as a time-averaged Heusler arrangement of Na ions and dynamically disordered NiH_5^{3-} complexes. This arrangement of metal atoms is shared with K_3ReH_6 which possesses ordered octahedral d^4 ReH_6^{3-} complexes.[62] Figure 5a displays an MD snapshot and the corresponding simulated diffraction pattern. Upon cooling, the reorientational dynamics of NiH_5^{3-} complexes arrest and subsequent ordering causes an orthorhombic distortion of the Na^+ counterion environment. To arrive at a model for the *Cmcm* structure, a range of trial structures with different orientations of NiH_5 complexes and Z = 4 were assembled inside a cubic simulation cell. DFT relaxation without using symmetry constraints yielded a robust lowest energy solution with orthorhombic lattice parameters very close to the experimentally observed ones and an atom arrangement with symmetry close to *Cmcm*. This is shown in Figure 5b, together with the simulated diffraction pattern. The structure parameters referring to a pressure of 5 GPa are given in Table 2.

The Rietveld refinement of HT-HP and LT-HP structures was repeated using the results of the computational simulations as starting models. The structure model for the refinement of the $Fm\bar{3}m$ HT-HP phase included Na atoms on 8c and 4b sites and Ni atoms occupying 4a sites. The hydrogen atoms were placed on a 48h Wyckoff site (and an occupancy of 5/12 was applied). This created a dodecahedral coordination around Ni atoms, which was intended to simulate the dynamically disordered situation. The Rietveld refinement was performed using the PXRD data collected at 365 °C (for the HT-HP phase) and at 320 °C and room temperature (for the *Cmcm* LT-HP phase), see Supporting Information for details about the refinement procedure. The refinements of the ∼5 GPa *in situ* data provided reasonable fits. The crystallographic results are given in Tables 3 and 4 as well as in Supporting Information, Figures S6 and S7.

Phase Stability of Na_3NiH_5 and the Electronic Structure of *Pnma* LP Na_3NiH_5. Next, we analyzed the phase and structure stability of polymorphic Na_3NiH_5 by DFT total energy calculations. Figure 6 shows $E-V$ and $\Delta H-p$ relations for the three phases of Na_3NiH_5 (referring to 0 K). Formation enthalpies ΔH were calculated with respect to NaH, Ni, and H_2. The HT-HP model corresponded to an MD snapshot which was relaxed in the considered volume range. The kink in the $E-V$ curve between 10 and 10.5 $Å^3$ is attributed to an orientation change of complexes. The enthalpy difference between the HT-HP and LT-HP phases can be estimated as 10 meV/atom (8.6 kJ/mol). The equilibrium volume for both phases is near 11.1 $Å^3$/atom (note that both phases have also very similar volumes at the experimental conditions of the phase transition, *cf.* Figure 2), whereas the calculated equilibrium volume for *Pnma* LP Na_3NiH_5 is 11.6 $Å^3$/atom. Below 1.5 GPa the *Pnma* phase is more stable than the *Cmcm* one, which is in reasonable agreement with the decompression experiment where the phase transformation was observed in the range 2.5−3 GPa at room temperature.

Figure 7 depicts the electronic structure of *Pnma* LP Na_3NiH_5 for the computed ambient pressure equilibrium structure (*cf.* Table 1). The occupied states in the electronic DOS mirror the MOs (and crystal field splitting) of an isolated, idealized, square pyramidal C_{4v} complex. The five bonding Ni−H σ-MOs possess the symmetry species $2A_1 + B_1 + E$ and would involve essentially $d_{x^2-y^2}$ (A_1) among the Ni d orbitals. The lowest lying band, centered at around −7 eV below the Fermi level, has essentially s character and translates to the $1a_1$ MO, and the remaining 4 Ni−H MOs are associated with states in the DOS region between −3 and −5 eV. The remaining occupied states, from about −2 eV up to the Fermi level, bear mainly Ni-d character. The narrow band at −2 eV is of nonbonding character and corresponds to a pure d_{xy} orbital (B_2), which is followed by weakly antibonding d_{xz}, d_{yz} (E) and d_{z^2} (A_1)-based bands. Thus, with five occupied (Ni−H) bonding and four occupied (Ni-d) nonbonding/weakly

Table 3. Results of the Rietveld Refinement of Na_3NiH_5 Polymorphs under Different p, T Conditions

phase	LP Na_3NiH_5	HT-HP Na_3NiH_5	LT-HP Na_3NiH_5	LT-HP Na_3NiH_5
temperature	RT (300 K)	365 °C (638 K)	320 °C (593 K)	RT (300 K)
pressure	ambient	∼5 GPa	∼5 GPa	∼4.4 GPa
crystal system	orthorhombic	cubic	orthorhombic	orthorhombic
space group	*Pnma* (62)	$Fm\bar{3}m$ (225)	*Cmcm* (63)	*Cmcm* (63)
Z	4	4	4	4
lattice parameters (Å)	a = 10.4131(9)	a = 7.16905(16)	a = 7.3444(9)	a = 7.3575(13)
	b = 7.3711(6)		b = 6.8828(9)	b = 6.7932(15)
	c = 5.4291(5)		c = 7.2247(8)	c = 7.2231(12)
V ($Å^3$)	416.71(6)	368.456(15)	365.21(8)	361.02(12)
V/Z ($Å^3$)	104.18	92.114	91.303	90.255
formula weight	132.7	132.7	132.7	132.7
d_{calc} (g/cm^3)	2.115	2.392	2.413	2.442
R_{obs} (%)	5.94	6.41	8.35	10.94
R_{all} (%)	5.94	6.41	8.71	11.10

Table 4. Fractional Coordinates and Atomic Displacement Parameters for the Various Na_3NiH_5 Polymorphs Obtained from Rietveld Refinement[a]

atom	site	*x*	*y*	*z*	U_{iso} (Å^2)
LP Na_3NiH_5 (Ambient, RT)					
Ni (Ni^{2+})	4*c*	0.8812(7)	0.25	0.7557(14)	0.0191(17)
Na1 (Na^+)	8*d*	0.1528(12)	0.0151(13)	0.8209(18)	0.025(3)
Na2 (Na^+)	4*c*	0.0731(13)	0.25	0.372(3)	0.025(3)
LT-HP Na_3NiH_5 (~5 GPa, 320 °C)					
Ni	4*c*	0	0.2427(15)	0.25	0.017(2)
Na1	8*e*	0.210(3)	0	0	0.070(6)
Na2	4*c*	0	0.691(4)	0.25	0.070(6)
LT-HP Na_3NiH_5 (~4.4 GPa, RT)					
Ni	4*c*	0	0.2391(16)	0.25	0.013(3)
Na1	8*e*	0.208(2)	0	0	0.046(6)
Na2	4*c*	0	0.675(3)	0.25	0.046(6)
HT-HP Na_3NiH_5 (~5 GPa, 365 °C)					
Ni	4*a*	0	0	0	0.0118(19)
Na1	8*c*	0.25	0.25	0.25	0.054(3)
Na2	4*b*	0.5	0.5	0.5	0.054(3)

[a] Hydrogen atoms for LP and LT-HP were introduced in the analysis from the DFT-optimized structures (Tables 1 and 2), and their positions were fixed during the refinement along with their ADPs [U_{iso} were set to 0.038 Å^2 (B_{iso} = 3 Å^2)]. H atoms for HT-HP were placed at a site 48*h* with x = 0.15 (Ni−H = 1.521 Å) and an occupancy of 5/12. See Supporting Information for Rietveld refinement procedures and resulting plots (Figures S6 and S7).

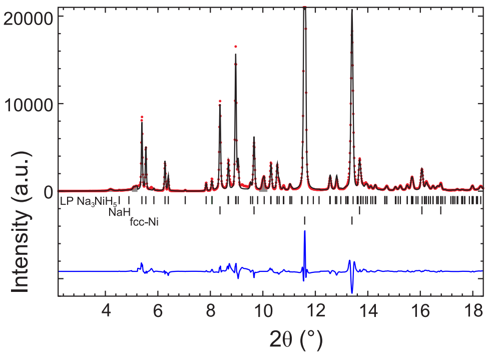

Figure 4. Rietveld fit of the DFT-optimized LP Na_3NiH_5 structure to the ambient synchrotron PXRD data of the product after depressurization of the 5 GPa run (λ = 0.41127 Å). Excluded regions are shown in gray (see Supporting Information for refinement details).

antibonding states per formula unit, one obtains the picture of NiH_5^{3-} as an 18-electron complex.

The highest lying occupied band, associated with the $3a_1$ (d_{z^2}) HOMO, has a considerable dispersion which diminishes the band gap. The calculated band gap has a very small size (about 0.2 eV) which may be underestimated as typical for DFT calculations. From the dark gray color of the sample (which may be caused by the presence of Ni), one cannot draw any conclusions on the presence and size of a band gap in LP Na_3NiH_5. Above the Fermi level, a band stretches from 0.2 to about 2.5 eV. This band is associated with the antibonding $2b_1$ LUMO, which completes the "1 over 4" crystal field splitting pattern of d orbitals for a C_{4v} complex.

Figure 8 shows the phonon DOS for *Pnma* LP Na_3NiH_5 for the computed ambient pressure equilibrium structure. The absence of imaginary modes manifests the dynamic stability of LP Na_3NiH_5. A square pyramidal C_{4v} complex will give rise to 12 internal modes, of which five are classified as stretching modes (2 × A_1, B_1, E) and seven as bending and deformations (A_1, B_1, B_2, 2 × E). In addition, each complex will produce three libration (torsion) modes in the solid. Accordingly, the H-based modes in Na_3NiH_5 will distribute over three regions. Ni−H stretches are between 1300 and 1900 cm^{-1}. The two symmetric stretches (A_1) may be distinguished as apical (involving the apical H-ligand) and basal (involving the four basal H-ligands). The basal stretch is at the highest wavenumber (1830 cm^{-1}), whereas the apical one is at the lowest (1350 cm^{-1}). Six out of seven Ni−H bending/deformation modes are in the wavenumber range 600−800 cm^{-1}. One deformation mode attains a very low wavenumber (400 cm^{-1}) and falls in the spectral region of the libration modes (200−400 cm^{-1}).

Because of the sensitivity of Na_3NiH_5 toward decomposition, we were not able to corroborate the vibrational modes suggested from the calculated phonon DOS by IR/Raman measurements. It is therefore instructive to compare with isoelectronic and isostructural CoH_5^{4-} and also NiH_4^{4-} for which vibrational properties have been reported earlier.[63,64] For CoH_5^{4-} in Mg_2CoH_5, Co−H stretches are in a range 1632−1834 cm^{-1}.[64] As in NiH_5^{3-}, the two symmetric stretches represent the extremes. However, the basal stretch is at considerably higher wavenumbers compared to NiH_5^{3-}. This is attributed to the large disparity of basal and apical Ni−H bond lengths. Bending modes for CoH_5^{4-} are between 766 and 1032 cm^{-1} and thus higher than for NiH_5^{3-}, which indicates that Co−H bonds are more rigid with respect to angular displacements. For NiH_4^{4-}, stretching and bending modes are at lower wavenumbers compared to CoH_5^{4-} (1674−1691 and 620−791 cm^{-1}) and thus are more comparable to NiH_5^{3-}.[63] The libration modes of Mg_2CoH_5 and Mg_2NiH_4 are at considerably higher wavenumbers (420−580 cm^{-1}) which is expected because the divalent, polarizing Mg^{2+} ions will create a more rigid torsional potential for the complex ions.

Formation of $NaNiH_3$ at p > 10 GPa and Its Recovery to Ambient Pressures. The investigation of the Na−Ni−H system was then extended to 10 GPa in order to further explore the polymorphic behavior of Na_3NiH_5 compounds and

https://dx.doi.org/10.1021/acsomega.0c00239
ACS Omega 2020, 5, 8730−8743

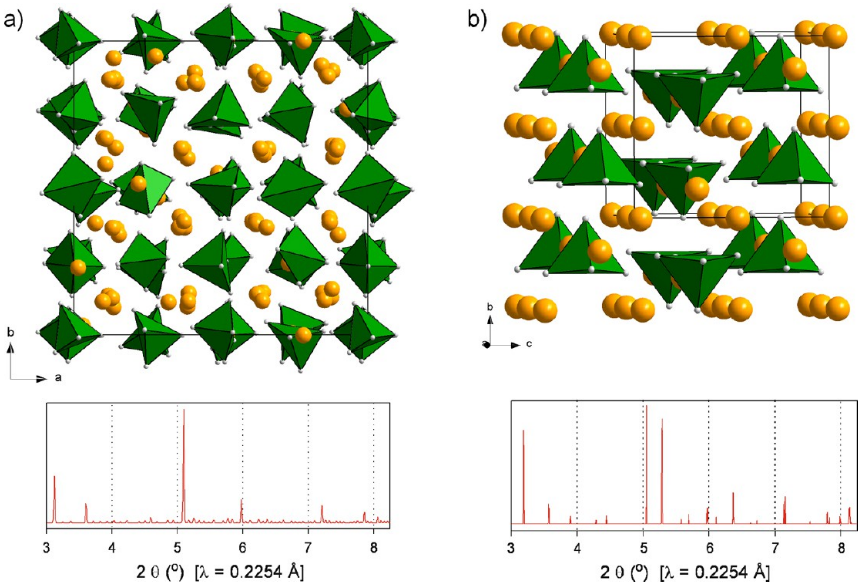

Figure 5. (a) $Z = 32$ MD snapshot of HT-HP Na_3NiH_5 at 1000 K (using the experimental volume at ~5 GPa and 510 °C) after equilibration (top) and calculated powder diffraction pattern (bottom). (b) DFT relaxed model of *Cmcm* LT-HP Na_3NiH_5 at 5 GPa (top) and calculated powder diffraction pattern (bottom). NiH_5^{3-} complexes are drawn as green polyhedra.

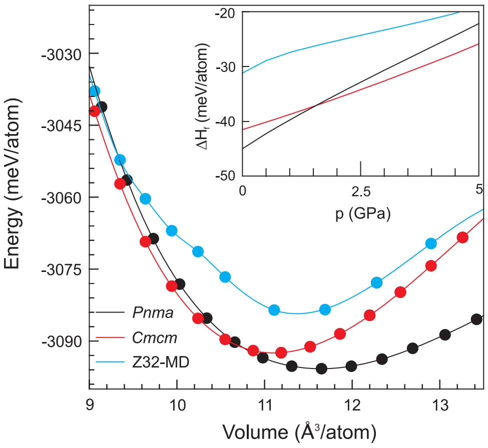

Figure 6. Total energy *vs* volume and formation enthalpy versus pressure relations of HT-HP Na_3NiH_5, *Cmcm* LT-HP Na_3NiH_5, and *Pnma* LP Na_3NiH_5. Formation enthalpies refer to $3NaH + Ni + H_2$.

the possibility of forming other Na−Ni−H phases. The sample was heated at a starting pressure of 10.4 GPa at which initial H_2 release and complete decomposition of BH_3NH_3 are expected at 260 and 310−330 °C, respectively.[26] The formation of γ-NiH became visible in PXRD patterns above 270 °C as a very diffuse peak near the 200 reflection of Ni (see upper part of Figure 9a). At 310 °C, the temperature was kept constant for about 35 min, after which heating was resumed at a slow rate (~4 °C/min). Similar to the 5 GPa experiments, at about 440 °C, the growth of HT-HP Na_3NiH_5 was noted. However, at lower temperatures (350−380 °C), a set of very faint additional peaks was detected in the PXRD patterns (marked with red arrows in Figure 9a). The intensities of these new peaks continued to increase during further heating. To observe the development of the two phases, the sample was kept at ~480 °C for ~80 min. Intensities of the diffraction peaks for both HT-HP Na_3NiH_5 and the new phase noticeably increased during this time.

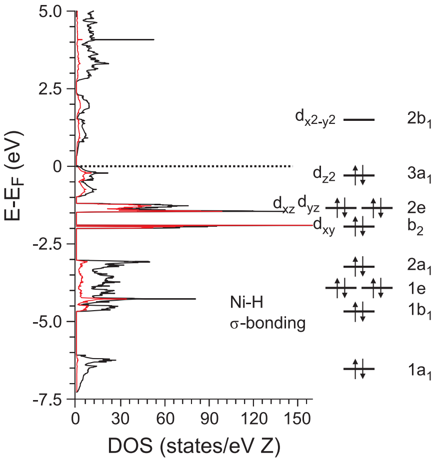

Figure 7. Electronic DOS of *Pnma* LP Na_3NiH_5 at the equilibrium volume corresponding to ambient pressure (left) and schematic MO diagram for the 18 electron complex, showing the sequence of 5 Ni−H σ-bonding orbitals, 4 nonbonding, d-based, orbitals and the antibonding lowest unoccupied molecular orbital (LUMO) (right). The latter maps the crystal field splitting of the d orbitals. (Total DOS: black line, Ni-partial DOS: red line. Energy is plotted with respect to the Fermi level, $E_F = 0$ eV).

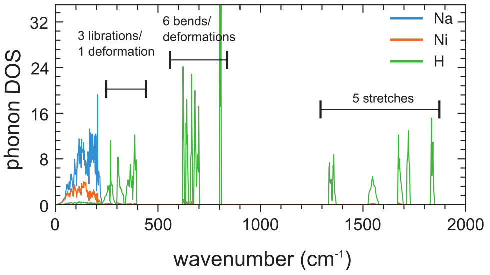

Figure 8. Phonon DOS (pDOS) of *Pnma* LP Na_3NiH_5 at the equilibrium volume corresponding to ambient pressure. pDOS is partitioned into atomic contributions of H, Na, and Ni.

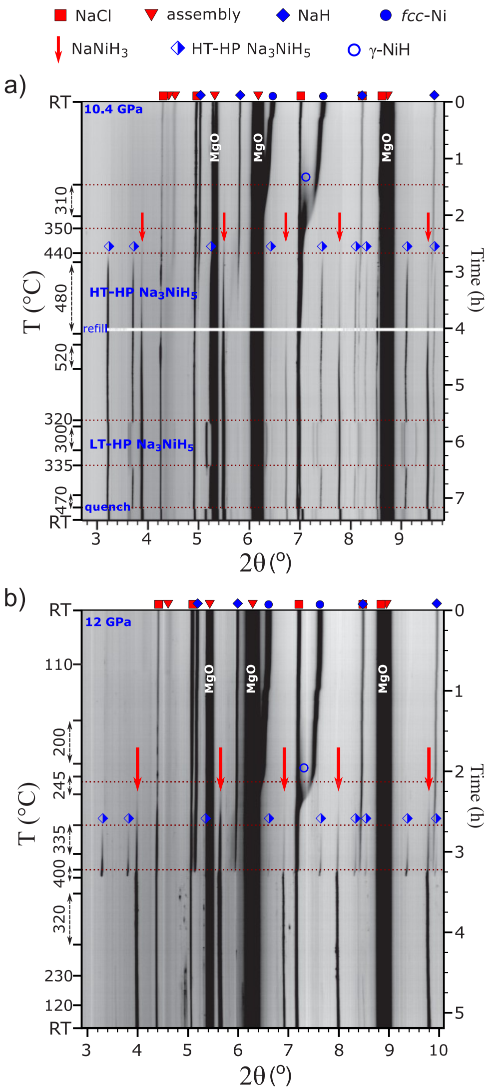

Figure 9. (a) Compilation of *in situ* PXRD patterns (λ = 0.22542 Å and 0.2296 Å, respectively) showing formation of ternary hydrides from a NaH/Ni/H_2 = 2:1:2.5 reaction mixture at around 10 (a) and 12 GPa (b). The diffraction peaks arising from the 14/8 and 10/5 multianvil assemblies (MgO, *h*-BN, $MgCr_2O_4$) are marked with red triangles.

The sample was further heated to 520 °C and then dwelled for 25 min. As a result, the reflections of the new phase became even more pronounced. To find out if the polymorphic behavior of the Na_3NiH_5 phase is preserved at ~10 GPa and to further observe the behavior of the new phase, the sample was cooled down to ~300 °C. The phase transition of HT-HP Na_3NiH_5 to the LT-HP polymorph occurred at ~320 °C, and upon reheating to 340 °C, the back-transformation was seen at ~335 °C. The temperature interval and rapid nature of the order−disorder transition closely mimicked the experiments at 5 GPa. During the course of these temperature variations, lasting for about 3 h, it appeared that the new phase grows slowly over time at the expense of the initially formed Na_3NiH_5 (*cf.* Figure S8, Supporting Information).

Afterward, the sample was heated to ~470 °C and subsequently temperature-quenched. As in the experiments at 5 GPa, the HT-HP phase underwent instant transformation to the orthorhombic LT-HP form on rapid cooling, whereas the diffraction peaks of the new phase remained unaltered. The pressure at room temperature was estimated as 8.9 GPa. The sample was then decompressed and recovered. PXRD characterization of the product revealed that the new compound was still present under ambient conditions, whereas LT-HP Na_3NiH_5 transformed to *Pnma* LP Na_3NiH_5, once again reproducing the behavior during the 5 GPa experiments.

The reflections of the new phase were indexed to a primitive cubic unit cell with no reflection conditions, and $Pm\bar{3}m$ space group was used for further evaluation. The unit cell parameter *a* varied within ~3.32−3.33 Å during the temperature variations of this experiment. Le Bail analysis and subsequent structure solution via Superflip[58] resulted in a CsCl-type 1Na:1Ni metal arrangement. The cell parameter under ambient conditions was estimated as ≈3.43 Å, and the cubic perovskite structure $NaNiH_3$ was assumed for the new phase. This was confirmed by subsequent DFT calculations, which reproduced closely this cell parameter for the theoretical equilibrium structure. Consequently, it is inferred that at ~10 GPa, Na_3NiH_5 is initially formed for kinetic reasons and then superseded by the more thermodynamically stable $NaNiH_3$. To further investigate the effect of pressure on $NaNiH_3$ formation, an experiment at 12 GPa was conducted.

The compilation of PXRD patterns at ~12 GPa is shown in Figure 9b. The H release behavior of BH_3NH_3 at pressures above 10 GPa has not been explicitly determined. We estimate that complete decomposition at 12 GPa occurs around 350 °C. Growth of γ-NiH became apparent during ~15 min dwell at ~245 °C. During the same temperature dwell, extremely weak reflections of the $NaNiH_3$ phase appeared in the diffraction patterns. These peaks became increasingly prominent upon further heating. At ~335 °C, the diffraction peaks of HT-HP Na_3NiH_5 also started to emerge in the PXRD patterns. At this point, the temperature was dwelled for 20 min, and during the dwell the intensities of reflections for both HT-HP Na_3NiH_5 and $NaNiH_3$ continued to increase. Their cell parameters under these conditions were estimated as ≈6.89 and ≈3.30 Å, respectively. When the heating was resumed and the estimated temperature reached 400 °C, diffraction peaks of HT-HP Na_3NiH_5, NaH, and γ-NiH almost instantly disappeared, while at the same time, the intensities of $NaNiH_3$ increased remarkably (lower part of Figure 9b). After a 5 min dwell at 400 °C, the sample was cooled to room temperature. No noticeable changes occurred to the $NaNiH_3$ pattern, and no other Na−Ni−H phases could be detected. At room temperature, the estimated pressure was 10.6 GPa. The cell parameter of $NaNiH_3$ after cooling corresponded to ≈3.295 Å.

The *in situ* PXRD data collected on decompression were further used to extract the unit cell volume of $NaNiH_3$ as a function of pressure. Figure S9 (Supporting Information) shows the pressure−volume EOS of $NaNiH_3$. The bulk modulus extracted from the experimental data is 69.9(1) GPa. This is somewhat lower than the DFT calculated value [80.8(4) GPa] and may indicate the presence of H defects in $NaNiH_3$, that is, $NaNiH_{3-\delta}$. H deficiency in transition metal perovskite hydrides is especially known for the Pd-based representatives $CaPdH_{3-\delta}$ and $SrPdH_{3-\delta}$ ($\delta \approx 0.1$).[65−67]

After the decompression, the sample was recovered for *ex situ* characterization. The sample color appeared brown with an orange tint and slight metallic luster. A high-resolution PXRD pattern confirmed $Pm\bar{3}m$ $NaNiH_3$ as the main product in the sample. The overall Rietveld fit is shown in Figure 10. A magnification of the high angle region and full width at half-maximum (FWHM) values for diffraction peaks as a function

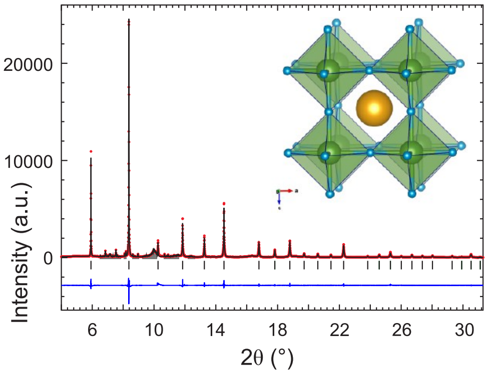

Figure 10. Rietveld fit of the $NaNiH_3$ cubic perovskite structure to the ambient synchrotron PXRD data of the product after depressurization of the 12 GPa run ($\lambda = 0.3544$ Å). Excluded regions are shown in gray (see Supporting Information for refinement details). Inset depicts the cubic perovskite structure.

of 2θ, strongly corroborating a cubic metric for $NaNiH_3$, are shown as Supporting Information, Figures S10 and S11. Refinement details are given in Table 5 and as Supporting Information, Table S1. The lattice parameter at ambient pressure and room temperature is a = 3.43235(3) Å which implies a Ni−H distance of 1.716 Å.

Table 5. Results of the Final Rietveld Refinement of the Perovskite $NaNiH_3$ Structure under Ambient Conditions

crystal system	cubic
space group	$Pm\bar{3}m$ (221)
Z	1
lattice parameters (Å)	$a = 3.43235(3)$
V (Å^3)	40.4365(6)
formula weight	84.7
d_{calc} (g/cm^3)	3.478
R_{obs} (%)	2.39
R_{all} (%)	2.39

Na−Ni−H System at High Pressures: Hydrido Complexes *Versus* Perovskite. *In situ* synchrotron diffraction studies revealed that rather moderate pressures, 5−12 GPa, readily afford the formation of compounds in the ternary Na−Ni−H system. In the hydrides identified, Na_3NiH_5 and $NaNiH_3$, Ni formally attains the oxidation state II. Polymorphic Na_3NiH_5 represents a (presumably) semiconducting CTMH constituting isolated complex ions NiH_5^{3-}. NiH_5^{3-} represents the first homoleptic hydrido complex in which Ni possesses an oxidation state larger than 0 and binds to more than four ligands. In contrast, the perovskite $NaNiH_3$ is metallic (see discussion below). Ni is octahedrally coordinated by six H ligands, which, however, are shared between two Ni centers. It has been shown earlier that T−H bonding in transition metal perovskite hydrides is pronouncedly covalent.[21,22] In this respect, the corner-sharing octahedron framework in $NaNiH_3$ should be considered as a polyanion, $[NiH_{6/3}]^-$, which is counterbalanced by Na^+ cations. Compared to Na_3NiH_5 with localized Ni−H single bonds (with lengths of 1.53, 1.55, and 1.67 Å), the Ni−H distance in $NaNiH_3$ (with delocalized Ni−H bonding) is longer, at 1.72 Å. The presence of both types of hydrides, CTMH and perovskite, within a single binary metal combination is very rare and has previously been only found for the Sr−Pd−H, Eu−Pd−H, and Ca−Rh−H systems.[67−70]

Figure 11 compares the (0 K) formation enthalpies of Na_3NiH_5 and $NaNiH_3$. Both systems are thermodynamically stable with respect to NaH + Ni + H_2, albeit weakly. The enthalpy change of the reactions $NaH + Ni + H_2 \rightarrow NaNiH_3$ and $3NaH + Ni + H_2 \rightarrow$ LP Na_3NiH_5 are estimated as −0.43 eV/Z (−41.5 kJ/mol) and −0.40 eV/Z (−38.6 kJ/mol), respectively, which is comparable to that of $LaNi_5$ hydrogenation (−32 kJ/mol H_2),[71] that is, high pressures are actually not required to stabilize these compounds. The significance of pressure for the synthesis of Na_3NiH_5 and $NaNiH_3$ is however two-fold. First, with pressure, the decomposition temperature will shift to higher values, thus enabling the application of elevated temperature for synthesis (>430 °C at ∼5 GPa and reduced to ∼300 °C at ∼12 GPa). Second, kinetic barriers—present at ambient pressure—will be substantially reduced with increasing pressure. Importantly, the pressure dependence of the activity of molecular hydrogen is not well known (and thus not considered in our calculations). However, at pressures above 1 GPa, the activity of molecular hydrogen increases sharply,[72,73] which generally favors hydride formation.

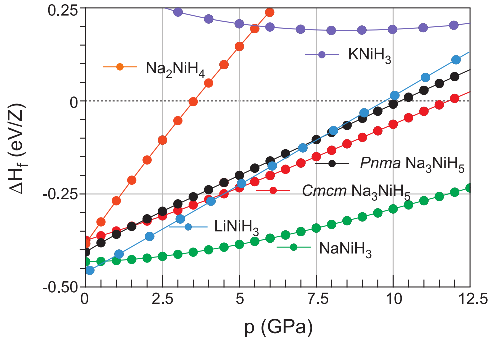

Figure 11. Compilation of formation enthalpies (with respect to NaH/*A*H + Ni + H_2) for *Pnma* LP Na_3NiH_5, *Cmcm* LT-HP Na_3NiH_5, Na_2NiH_4, and the perovskites $ANiH_3$ (A = Li, Na, K).

The calculated formation enthalpies also suggest that the formation of Na_3NiH_5 is kinetically driven. The decomposition according to $Na_3NiH_5 \rightarrow NaNiH_3 + 2NaH$ is favored at ambient pressure and becomes increasingly favorable with increasing pressure. Computed decomposition enthalpies as a function of pressure are shown in Figure S12 (Supporting Information). In Figure 11, we also included the formation enthalpy for hypothetical Na_2NiH_4 with the Na_2PtH_4 structure and square planar d^8-NiH_4^{2-} complexes.[74] At ambient pressure, Na_2NiH_4 appears similarly stable as Na_3NiH_5 but becomes rapidly disfavored with increasing pressure.

Transition metal perovskite hydrides are elusive. Including $NaNiH_3$ from this work, there are 10 known representatives. Most correspond to combinations of Ni and Pd with the divalent cations Ca, Sr, and Eu.[75] Lately, representatives with Co and Rh have been reported.[70,75] The electronic structure of transition metal perovskite hydrides has been analyzed earlier.[21,76,77] Figure 12a depicts the band structure of $NaNiH_3$ at the computed equilibrium volume. Spin-polarized calculations revealed a nonmagnetic ground state. Occupied bands are divided into bonding a_{1g} and e_g, nonbonding t_{2g}, and antibonding e_g^*. The weakly dispersed t_{2g} band is completely filled for 12 e/Z. Accordingly, in $NaNiH_3$ with 14 e/Z, the e_g^*

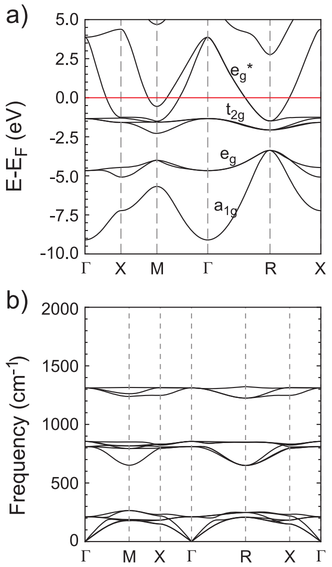

Figure 12. Electronic DOS (a) and phonon dispersion (b) for $NaNiH_3$ at zero pressure.

band is half-filled. The dispersion range of the Ni−H bonding and nonbonding bands relates well to the energy range of corresponding states for Na_3NiH_5 (*cf.* Figure 7). As initially mentioned, Ni−H bonding in $NaNiH_3$ is considered pronouncedly covalent. In this respect, it is instructive to discuss the result of a Bader analysis of charge densities[49] for the CTMHs LP Na_3NiH_5 and hypothetical Na_2NiH_4 with metallic $NaNiH_3$ and the ionic hydride NaH (NaCl-type). This is compiled in Table 6. Na attains a very similar (positive) charge, >0.8, irrespective of the system, which corroborates its cationic, Na^+, character in all systems. Na−H distances are at 2.43 and 2.45 Å for $NaNiH_3$ and NaH, respectively, and in a range 2.45−2.81 Å for LP Na_3NiH_5. Compared to NaH, constituting hydridic H^-, Bader charges and volumes for H are considerably smaller in the Na−Ni−H materials with covalent Ni−H bonding. Yet, the state of covalent bonding, localized and delocalized (metallic), can be discriminated. The perovskite is distinguished by small volumes of all constituting atoms, manifesting its compact structure.

Table 6. Compilation of Bader Charges and Volumes (Å^3)

compound	Na charge	Na volume	Ni charge	Ni volume	H charge	H volume
NaH	0.848	9.928			−0.848	17.824
$NaNiH_3$	0.838	7.503	0.366	12.531	−0.401	6.374
Na_2NiH_4	0.841	9.622	0.323	19.633	−0.502	11.78
Na_3NiH_5	0.824	9.947	0.224	15.190	−0.539	11.95

Figure 12b depicts the phonon dispersions of $NaNiH_3$ at the computationally relaxed equilibrium volume. The 5 atoms in the unit cell give rise to 12 optic modes, of which 3 are Ni−H stretches and 6 are Ni−H bends and the remaining 3 correspond to Na translations. The H stretching modes are around 1300 cm^{-1}, which is considerably lower than the Ni−H stretches in LP Na_3NiH_5 (1350−1850 cm^{-1}) because of the larger Ni−H bond length in the perovskite (*cf.* Figure 8). The bending modes, however, are in a similar range, 600−800 cm^{-1}. Computation of the Eliashberg function and electron−phonon coupling integral show that electron−phonon coupling is negligible in $NaNiH_3$, and thus, superconductivity is not expected.

With respect to Na_3NiH_5, the formation of more stable $NaNiH_3$ is kinetically hindered. Here, it is important to compare with the Li−Ni−H system for which the perovskite $LiNiH_3$ was recently reported.[23,76] Similar to $NaNiH_3$, $LiNiH_3$ was obtained from the reaction of LiH and Ni at high pressures in the presence of H_2 fluid. However, this reaction already occurred at pressures around 3 GPa via an intermediate $Li_yNi_{1-y}H$ solid solution (based on γ-NiH). There was no evidence for complex hydride formation in the Li−Ni−H system. Possibly, CTMH formation is suppressed because $Li_yNi_{1-y}H$ enables a more favorable kinetics for $LiNiH_3$ formation.

As included in Figure 11, the formation enthalpy of $LiNiH_3$ is very similar to $NaNiH_3$ at ambient and slightly elevated pressures, but $LiNiH_3$ is destabilized considerably with respect to $NaNiH_3$ with increasing pressure. Because of the small size of Li, the equilibrium lattice parameter of $LiNiH_3$ is very small, 3.266(1) Å (*cf.* ≈3.432 Å for $NaNiH_3$). Accordingly, the Ni−H distance within the octahedral framework is reduced to ≈1.633 Å, which is comparable to the apical Ni−H distance in Na_3NiH_5. A further decrease of the Ni−H distance by external pressure will then destabilize $LiNiH_3$ with respect to $NaNiH_3$.

Despite the small Ni−H distance in $LiNiH_3$, Li^+ remains loosely coordinated in the cuboctahedral cavity of the perovskite structure. Whereas the electronic structure of $LiNiH_3$ is very similar to $NaNiH_3$ (*cf.* refs 76 and 77), phonon dispersions are rather different. In particular, the loose Li−H coordination is revealed in the Ni−H bends which are at considerably lower wavenumbers compared to $NaNiH_3$ (by 150 cm^{-1} at Γ) and show a large dispersion, even merging with the phonons of Li translations at M and R (this is shown in Supporting Information, Figure S13). $LiNiH_3$ is clearly outside the Goldschmidt stability field for perovskite hydrides, as established by Ikeda et al.[75] Yet, its formation enthalpy is similar to $NaNiH_3$ which is situated inside the Goldschmidt stability field. In this respect, it is interesting to also investigate $KNiH_3$ which despite the considerably larger radius for K^+ (1.64 Å as compared to 1.39 Å for Na^+)[78] would also be located within the stability field. Again, the result is included in Figure 11. $KNiH_3$ has a positive formation energy for all pressures and is thus not expected to be thermodynamically stable. Note that $KNiH_3$ has a negative formation energy with respect to the elements, K + Ni + 3/2H_2.[77]

Because transition metal perovskite hydrides are expected to be stable only as 14 and 15 e/Z systems,[21,22,76] an interplay between complex hydride and perovskite formation will be limited to hydrides of transition metals from groups 9 and 10. For Na−Ni−H, the CTMH Na_3NiH_5 forms initially but is unstable toward decomposition to the perovskite according to $Na_3NiH_5 \rightarrow 2NaH + NaNiH_3$. In both forms of hydrides, Ni is present in the oxidation state II. A related interplay example has been reported for Ca−Rh−H. Here, Ca_2RhH_{5+x} is obtained from sintering mixtures of CaH_2 and Rh at temperatures between 250 and 500 °C in a slightly pressurized hydrogen atmosphere (several bars).[79,80] Mixed-valent Ca_2RhH_{5+x} ($x \approx 0.4$) crystallizes with a hydrogen-disordered K_2PtCl_6 structure, featuring locally isolated octahedral Rh(II)-H_6^{4-} and square pyramidal Rh(I)H_5^{4-} complexes. Furthermore, this synthesis strategy afforded also the more Rh-rich phases $Ca_8Rh_5H_{25}$ and $Ca_8Rh_6H_{24}$ in which additional Rh atoms are inserted in the K_2PtCl_6 structure and link previously

https://dx.doi.org/10.1021/acsomega.0c00239
ACS Omega 2020, 5, 8730−8743

isolated complexes through common H ligands. It has been conjectured that these more Rh-rich phases represent intermediates toward the perovskite $CaRhH_3$ according to $Ca_2Rh(II)H_6$ + Rh = 2 $CaRh(I)H_3$.[79] The synthesis of $CaRhH_3$ has not yet been achieved from reaction mixtures CaH_2 + Rh + H_2, and we suspect that, similar to $NaNiH_3$, its formation via $Ca_2Rh_{1+x}H_{6-y}$ CTMHs is kinetically hindered but should be possible when using high pressures. Recently, the Kohlmann group reported the synthesis of $CaRhH_3$ from a different route, $CaRh_2 + H_2 = CaRhH_3 + Rh$, using the Laves phase $CaRh_2$ as a precursor.[70] This hydrogenation reaction proceeds under comparatively mild conditions, ~250 °C and 50 bar H_2 pressure.

Metallic transition metal hydride perovskites have been investigated for superconductivity early on. Orgaz et al. performed a computational study on the electron−phonon coupling in the Pd hydrides $MPdH_3$ (M = Ca, Sr, Eu, and Yb) but found only moderate to weak coupling, suggesting low values of the superconducting transition temperature.[81] Indeed, Ayukawa et al. did not observe superconductivity for $CaPdH_{3-\delta}$ above 2 K.[66] The superconducting properties of Ni hydride perovskites and $CaRhH_3$ are not known. Our calculations, however, indicate only a very weak electron−phonon coupling in $NaNiH_3$, and thus, superconductivity above 2 K is not expected.

■ CONCLUSIONS

The application of high pressures afforded for the first time ternary compounds in the Na−Ni−H system. Polymorphic Na_3NiH_5 featuring square pyramidal complex ions NiH_5^{3-} was obtained from reaction mixtures NaH−Ni−H_2 at pressures between 5 and 10 GPa. NiH_5^{3-} represents the first homoleptic hydrido complex in which Ni possesses an oxidation state larger than 0 and binds to more than four ligands. At temperatures above ~335 °C, Na_3NiH_5 adopts a *fcc* structure in which NiH_5^{3-} complexes are dynamically disordered (HT-HP Na_3NiH_5); at lower temperatures, the structure distorts orthorhombically and complexes appear ordered (LT-HP Na_3NiH_5). Upon pressure release, LT-HP Na_3NiH_5 undergoes a phase transition to a low pressure form (LP Na_3NiH_5) which can be recovered at ambient p, T. Na_3NiH_5 is unstable with respect to decomposition into the perovskite $NaNiH_3$, according to $Na_3NiH_5 \rightarrow NaNiH_3 + 2NaH$, and it is inferred that its formation is kinetically driven. $NaNiH_3$, in which Ni is octahedrally coordinated by six H atoms, was obtained at pressures 10−12 GPa. Also, this ternary hydride phase can be recovered at ambient conditions. It is conjectured that with pressure, a similar interplay between complex hydride and perovskite phases can be observed in the CaH_2−Rh−H_2 system. Na_3NiH_5 and $NaNiH_3$ are further examples of ternary hydrogen-rich hydrides that form under comparatively low pressure conditions and can be retained at ambient pressure.

■ ASSOCIATED CONTENT

Supporting Information

The Supporting Information is available free of charge at https://pubs.acs.org/doi/10.1021/acsomega.0c00239.

Splitting of 220 reflection during the transition of HT-HP Na_3NiH_5 to LT-HP polymorph, formation of LP Na_3NiH_5 polymorph upon decompression of the 5 GPa run at RT, fragment of a 2D-PXRD pattern of the recovered LP Na_3NiH_5 product, deviatoric stress as a function of the simulation time for HT-HP Na_3NiH_5, probability map of angular positions of H atoms in NiH_5^{3-} complexes in the HT-HP and LT-HP phases, results of the Rietveld fit of the cubic HT-HP Na_3NiH_5 and the *Cmcm* LT-HP Na_3NiH_5 models to *in situ* PXRD data, results of the Rietveld fit of the *Cmcm* LT-HP Na_3NiH_5 model, changes in phase fractions of Na−Ni−H products and nickel hydride during 10 GPa run, experimental and computed EOS for $NaNiH_3$, magnified high angle region of the $NaNiH_3$ perovskite structure Rietveld fit, FWHM values for $NaNiH_3$ diffraction peaks as a function of 2θ at ambient p, T, DFT-computed decomposition enthalpies for Na_3NiH_5 and Na_2NiH_4, comparison of the electronic band structure and phonon dispersions for $NaNiH_3$ and $LiNiH_3$, fractional coordinates and atomic displacement parameters obtained for the perovskite $NaNiH_3$, and details of the structure solution of the "Na_3Ni" arrangement for LP Na_3NiH_5 and the Rietveld refinement procedure for Na−Ni−H products (PDF)

Crystallographic data of LP Na_3NiH_5 at ambient p, T (CIF)

Crystallographic data of HT-HP Na_3NiH_5 at 638 K and ~5 GPa (CIF)

Crystallographic data of LT-HP Na_3NiH_5 at 593 K and ~5 GPa (CIF)

Crystallographic data of LT-HP Na_3NiH_5 at RT and ~4.4 GPa (CIF)

Crystallographic data of perovskite $NaNiH_3$ at ambient p, T (CIF)

■ AUTHOR INFORMATION

Corresponding Authors

Kristina Spektor − *ESRF, The European Synchrotron Radiation Facility, F-38000 Grenoble, France;* orcid.org/0000-0002-3267-9797; Email: Kristina.Spektor@gmail.com

Ulrich Häussermann − *Department of Materials and Environmental Chemistry, Stockholm University, SE-10691 Stockholm, Sweden;* orcid.org/0000-0003-2001-4410; Email: Ulrich.Haussermann@mmk.su.se

Authors

Wilson A. Crichton − *ESRF, The European Synchrotron Radiation Facility, F-38000 Grenoble, France*

Stanislav Filippov − *Theoretical Physics Division, Department of Physics, Chemistry and Biology (IFM), Linköping University, SE-581 83 Linköping, Sweden; Department of Materials and Environmental Chemistry, Stockholm University, SE-10691 Stockholm, Sweden*

Johan Klarbring − *Theoretical Physics Division, Department of Physics, Chemistry and Biology (IFM), Linköping University, SE-581 83 Linköping, Sweden*

Sergei I. Simak − *Theoretical Physics Division, Department of Physics, Chemistry and Biology (IFM), Linköping University, SE-581 83 Linköping, Sweden*

Andreas Fischer − *Department of Physics, Augsburg University, D-86135 Augsburg, Germany*

Complete contact information is available at: https://pubs.acs.org/10.1021/acsomega.0c00239

Notes

The authors declare no competing financial interest.

■ ACKNOWLEDGMENTS

The ESRF is thanked for allocating the beamtime CH-4899 and in-house research time at beamline ID06LVP. K.S. would like to thank Michael Hanfland for the help with measurements at beamline ID15B, Andrew Fitch and Catherine Dejoie for performing the high-resolution PXRD measurement at ID22, and Harald Müller for assistance with the Chemistry Laboratory facilities at ESRF. S.I.S. acknowledges support from the Swedish Research Council (VR) (Project No. 2019-05551) and the Swedish Government Strategic Research Area in Materials Science on Advanced Functional Materials at at Linköping University (Faculty Grant SFO-Mat-LiU No. 2009-00971). S.F. acknowledges the financial support from Carl Tryggers Stiftelse (CTS) för Vetenskaplig Forskning through grants 16:198 and 17:206. The computations were performed on resources provided by the Swedish National Infrastructure for Computing (SNIC) at High Performance Computing Center North (HPC2N).

■ REFERENCES

(1) Drozdov, A. P.; Eremets, M. I.; Troyan, I. A.; Ksenofontov, V.; Shylin, S. I. Conventional Superconductivity at 203 Kelvin at High Pressures in the Sulfur Hydride System. *Nature* **2015**, *525*, 73−76.

(2) Duan, D.; Liu, Y.; Ma, Y.; Shao, Z.; Liu, B.; Cui, T. Structure and Superconductivity of Hydrides at High Pressures. *Natl. Sci. Rev.* **2017**, *4*, 121−135.

(3) Wang, H.; Li, X.; Gao, G.; Li, Y.; Ma, Y. Hydrogen-rich superconductors at high pressures. *Wiley Interdiscip. Rev.: Comput. Mol. Sci.* **2018**, *8*, No. e1330.

(4) Boeri, L.; Bachelet, G. B. Viewpoint: The Road to Room-Temperature Conventional Superconductivity. *J. Phys.: Condens. Matter* **2019**, *31*, 234002.

(5) Zurek, E.; Bi, T. High-Temperature Superconductivity in Alkaline and Rare Earth Polyhydrides at High Pressure: A Theoretical Perspective. *J. Chem. Phys.* **2019**, *150*, 050901.

(6) Wang, H.; Tse, J. S.; Tanaka, K.; Iitaka, T.; Ma, Y. Superconductive Sodalite-like Clathrate Calcium Hydride at High Pressures. *Proc. Natl. Acad. Sci. U.S.A.* **2012**, *109*, 6463−6466.

(7) Liu, H.; Naumov, I. I.; Hoffmann, R.; Ashcroft, N. W.; Hemley, R. J. Potential high-T_c superconducting lanthanum and yttrium hydrides at high pressure. *Proc. Natl. Acad. Sci. U.S.A.* **2017**, *114*, 6990−6995.

(8) Geballe, Z. M.; Liu, H.; Mishra, A. K.; Ahart, M.; Somayazulu, M.; Meng, Y.; Baldini, M.; Hemley, R. J. Synthesis and Stability of Lanthanum Superhydrides. *Angew. Chem., Int. Ed.* **2018**, *57*, 688−692.

(9) Struzhkin, V. V.; Kim, D. Y.; Stavrou, E.; Muramatsu, T.; Mao, H.-k.; Pickard, C. J.; Needs, R. J.; Prakapenka, V. B.; Goncharov, A. F. Synthesis of Sodium Polyhydrides at High Pressures. *Nat. Commun.* **2016**, *7*, 12267.

(10) Pépin, C. M.; Geneste, G.; Dewaele, A.; Mezouar, M.; Loubeyre, P. Synthesis of FeH_5: A Layered Structure with Atomic Hydrogen Slabs. *Science* **2017**, *357*, 382−385.

(11) Takagi, S.; Iijima, Y.; Sato, T.; Saitoh, H.; Ikeda, K.; Otomo, T.; Miwa, K.; Ikeshoji, T.; Aoki, K.; Orimo, S.-i. True Boundary for the Formation of Homoleptic Transition-Metal Hydride Complexes. *Angew. Chem., Int. Ed.* **2015**, *54*, 5650−5653.

(12) Takagi, S.; Orimo, S.-i. Recent Progress in Hydrogen-Rich Materials from the Perspective of Bonding Flexibility of Hydrogen. *Scr. Mater.* **2015**, *109*, 1−5.

(13) Takagi, S.; Iijima, Y.; Sato, T.; Saitoh, H.; Ikeda, K.; Otomo, T.; Miwa, K.; Ikeshoji, T.; Orimo, S.-i. Formation of Novel Transition Metal Hydride Complexes with Ninefold Hydrogen Coordination. *Sci. Rep.* **2017**, *7*, 44253.

(14) Antonov, V. E. Phase Transformations, Crystal and Magnetic Structures of High-Pressure Hydrides of *d*-Metals. *J. Alloys Compd.* **2002**, *330−332*, 110−116.

(15) Fukai, Y. The structure and phase diagram of M-H systems at high chemical potentials-High pressure and electrochemical synthesis. *J. Alloys Compd.* **2005**, *404−406*, 7−15.

(16) Baranowski, B.; Filipek, S. M. 45 Years of nickel hydride-History and perspectives. *J. Alloys Compd.* **2005**, *404−406*, 2−6.

(17) Ying, J.; Liu, H.; Greenberg, E.; Prakapenka, V. B.; Struzhkin, V. V. Synthesis of New Nickel Hydrides at High Pressure. *Phys. Rev. Mater.* **2018**, *2*, 085409.

(18) Schlapbach, L.; Züttel, A. Hydrogen-Storage Materials for Mobile Applications. *Nature* **2001**, *414*, 353−358.

(19) Züttel, A. Hydrogen Storage Methods. *Naturwissenschaften* **2004**, *91*, 157−172.

(20) Takeshita, H. T.; Oishi, T.; Kuriyama, N. Disproportionation of $CaNi_3$ hydride: formation of new hydride, $CaNiH_3$. *J. Alloys Compd.* **2002**, *333*, 266−273.

(21) Sato, T.; Noréus, D.; Takeshita, H.; Häussermann, U. Hydrides with the Perovskite Structure: General Bonding and Stability Considerations and the New Representative $CaNiH_3$. *J. Solid State Chem.* **2005**, *178*, 3381−3388.

(22) Ikeda, K.; Sato, T.; Orimo, S.-i. Perovskite-type hydrides - synthesis, structures and properties. *Int. J. Mater. Res.* **2008**, *99*, 471−479.

(23) Sato, R.; Saitoh, H.; Endo, N.; Takagi, S.; Matsuo, M.; Aoki, K.; Orimo, S.-i. Formation Process of Perovskite-Type Hydride $LiNiH_3$: In Situ Synchrotron Radiation X-Ray Diffraction Study. *Appl. Phys. Lett.* **2013**, *102*, 091901.

(24) Yvon, K.; Renaudin, G. Hydrides: Solid State Transition Metal Complexes. *Encyclopedia of Inorganic Chemistry*; John Wiley & Sons, Ltd, 2006.

(25) Bronger, W.; Auffermann, G. New Ternary Alkali-Metal−Transition-Metal Hydrides Synthesized at High Pressures: Characterization and Properties. *Chem. Mater.* **1998**, *10*, 2723−2732.

(26) Nylén, J.; Sato, T.; Soignard, E.; Yarger, J. L.; Stoyanov, E.; Häussermann, U. Thermal Decomposition of Ammonia Borane at High Pressures. *J. Chem. Phys.* **2009**, *131*, 104506.

(27) Spektor, K.; Crichton, W. A.; Konar, S.; Filippov, S.; Klarbring, J.; Simak, S. I.; Häussermann, U. Unraveling Hidden Mg−Mn−H Phase Relations at High Pressures and Temperatures by in Situ Synchrotron Diffraction. *Inorg. Chem.* **2018**, *57*, 1614−1622.

(28) Guignard, J.; Crichton, W. A. The Large Volume Press Facility at ID06 Beamline of the European Synchrotron Radiation Facility as a High Pressure-High Temperature Deformation Apparatus. *Rev. Sci. Instrum.* **2015**, *86*, 085112.

(29) Birch, F. Equation of State and Thermodynamic Parameters of NaCl to 300 Kbar in the High-Temperature Domain. *J. Geophys. Res.: Solid Earth* **1986**, *91*, 4949−4954.

(30) Nishihara, Y.; Doi, S.; Kakizawa, S.; Higo, Y.; Tange, Y. Effect of Pressure on Temperature Measurements Using WRe Thermocouple and Its Geophysical Impact. *Phys. Earth Planet. Inter.* **2020**, *298*, 106348.

(31) Errandonea, D. High-Pressure Melting Curves of the Transition Metals Cu, Ni, Pd, and Pt. *Phys. Rev. B* **2013**, *87*, 054108.

(32) Lord, O. T.; Wood, I. G.; Dobson, D. P.; Vočadlo, L.; Wang, W.; Thomson, A. R.; Wann, E. T. H.; Morard, G.; Mezouar, M.; Walter, M. J. The Melting Curve of Ni to 1 Mbar. *Earth Planet. Sci. Lett.* **2014**, *408*, 226−236.

(33) Hammersley, A. P. FIT2D: A Multi-Purpose Data Reduction, Analysis and Visualization Program. *J. Appl. Crystallogr.* **2016**, *49*, 646−652.

(34) Hammersley, A. P.; Riekel, C. MFIT: Multiple Spectra Fitting Program. *Synchrotron Radiat. News* **1989**, *2*, 24−26.

(35) Shirley, R. *Crysfire 2004: An Interactive Powder Indexing Support System*: 41 Guildford Park Avenue, Guildford, Surrey, U.K., 2004.

(36) Hammersley, A. P.; Svensson, S. O.; Hanfland, M.; Fitch, A. N.; Hausermann, D. Two-Dimensional Detector Software: From Real Detector to Idealised Image or Two-Theta Scan. *High Pressure Res.* **1996**, *14*, 235−248.

(37) Le Bail, A.; Duroy, H.; Fourquet, J. L. Ab-initio structure determination of $LiSbWO_6$ by X-ray powder diffraction. *Mater. Res. Bull.* **1988**, *23*, 447−452.

(38) Rietveld, H. M. A Profile Refinement Method for Nuclear and Magnetic Structures. *J. Appl. Crystallogr.* **1969**, *2*, 65−71.

(39) Petříček, V.; Dušek, M.; Palatinus, L. Crystallographic Computing System JANA2006: General Features. *Z. Kristallogr. - Cryst. Mater.* **2014**, *229*, 345−352.

(40) Angel, R. J. Equations of State. *Rev. Mineral. Geochem.* **2000**, *41*, 35−59.

(41) Kresse, G.; Hafner, J. *Ab initio* molecular dynamics for liquid metals. *Phys. Rev. B* **1993**, *47*, 558−561.

(42) Kresse, G.; Furthmüller, J. Efficient iterative schemes for *ab initio* total-energy calculations using a plane-wave basis set. *Phys. Rev. B* **1996**, *54*, 11169.

(43) Blöchl, P. E. Projector Augmented-Wave Method. *Phys. Rev. B* **1994**, *50*, 17953−17979.

(44) Kresse, G.; Joubert, D. From Ultrasoft Pseudopotentials to the Projector Augmented-Wave Method. *Phys. Rev. B* **1999**, *59*, 1758.

(45) Perdew, J. P.; Burke, K.; Ernzerhof, M. Generalized Gradient Approximation Made Simple. *Phys. Rev. Lett.* **1996**, *77*, 3865−3868.

(46) Perdew, J. P.; Burke, K.; Ernzerhof, M. Generalized Gradient Approximation Made Simple [Phys. Rev. Lett. 77, 3865 (1996)]. *Phys. Rev. Lett.* **1997**, *78*, 1396.

(47) Monkhorst, H. J.; Pack, J. D. Special Points for Brillouin-Zone Integrations. *Phys. Rev. B* **1976**, *13*, 5188−5192.

(48) Blöchl, P. E.; Jepsen, O.; Andersen, O. K. Improved Tetrahedron Method for Brillouin-Zone Integrations. *Phys. Rev. B* **1994**, *49*, 16223−16233.

(49) Bader, R. F. W. *Atoms in Molecules: A Quantum Theory*; Oxford University Press: Oxford, 1990.

(50) Arnaldsson, A.; Tang, W.; Chill, S.; Chai, W.; Henkelman, G. Code: Bader Charge Analysis. http://theory.cm.utexas.edu/henkelman/code/bader/ (accessed April 4, 2020).

(51) Henkelman, G.; Arnaldsson, A.; Jónsson, H. A Fast and Robust Algorithm for Bader Decomposition of Charge Density. *Comput. Mater. Sci.* **2006**, *36*, 354−360.

(52) Kresse, G.; Furthmüller, J.; Hafner, J. Ab Initio Force Constant Approach to Phonon Dispersion Relations of Diamond and Graphite. *Europhys. Lett.* **1995**, *32*, 729−734.

(53) Parlinski, K.; Li, Z. Q.; Kawazoe, Y. First-Principles Determination of the Soft Mode in Cubic ZrO_2. *Phys. Rev. Lett.* **1997**, *78*, 4063−4066.

(54) Togo, A.; Tanaka, I. First Principles Phonon Calculations in Materials Science. *Scr. Mater.* **2015**, *108*, 1−5.

(55) Giannozzi, P.; Baroni, S.; Bonini, N.; Calandra, M.; Car, R.; Cavazzoni, C.; Ceresoli, D.; Chiarotti, G. L.; Cococcioni, M.; Dabo, I.; et al. QUANTUM ESPRESSO: A Modular and Open-Source Software Project for Quantum Simulations of Materials. *J. Phys.: Condens. Matter* **2009**, *21*, 395502.

(56) Giannozzi, P.; Andreussi, O.; Brumme, T.; Bunau, O.; Buongiorno Nardelli, M.; Calandra, M.; Car, R.; Cavazzoni, C.; Ceresoli, D.; Cococcioni, M.; et al. Advanced Capabilities for Materials Modelling with Quantum ESPRESSO. *J. Phys.: Condens. Matter* **2017**, *29*, 465901.

(57) Allen, P. B.; Dynes, R. C. Transition Temperature of Strong-Coupled Superconductors Reanalyzed. *Phys. Rev. B* **1975**, *12*, 905−922.

(58) Palatinus, L.; Chapuis, G. SUPERFLIP- a computer program for the solution of crystal structures by charge flipping in arbitrary dimensions. *J. Appl. Crystallogr.* **2007**, *40*, 786−790.

(59) Bremm, T.; Jansen, M. Einkristallzüchtung und Strukturanalyse von Trikaliumorthonitrat. *Z. Anorg. Allg. Chem.* **1992**, *608*, 56−59.

(60) Endeavour − Structure Solution from Powder Diffraction. Crystal Impact; Dr. H. Putz & Dr. K. Brandenburg GbR: Bonn, Germany, http://www.crystalimpact.com/endeavour (accessed April 4, 2020).

(61) Zolliker, P.; Yvon, K.; Fischer, P.; Schefer, J. Dimagnesium Cobalt (I) Pentahydride, Mg_2CoH_5, Containing Square-Pyramidal Pentahydrocobaltate CoH_5^{4-} Anions. *Inorg. Chem.* **1985**, *24*, 4177−4180.

(62) Bronger, W.; Auffermann, G.; Schilder, H. K_3ReH_6− Synthese, Struktur und magnetische Eigenschaften. *Z. Anorg. Allg. Chem.* **1998**, *624*, 497−500.

(63) Parker, S. F. Spectroscopy and bonding in ternary metal hydride complexes-Potential hydrogen storage media. *Coord. Chem. Rev.* **2010**, *254*, 215−234.

(64) Parker, S. F.; Jayasooriya, U. A.; Sprunt, J. C.; Bortz, M.; Yvon, K. Inelastic Neutron Scattering, IR and Raman Spectroscopic Studies of Mg_2CoH_5 and Mg_2CoD_5. *J. Chem. Soc., Faraday Trans.* **1998**, *94*, 2595−2599.

(65) Bronger, W.; Jansen, K.; Müller, P. $CaPdH_2$, ein ternäres hydrid mit perowskitverwandter struktur. *J. Less-Common Met.* **1990**, *161*, 299−302.

(66) Ayukawa, S.-y.; Ikeda, K.; Kato, M.; Noji, T.; Orimo, S.-i.; Koike, Y. Synthesis and Specific Heat of $CaPdH_{3-\delta}$ with the Perovskite Structure. *J. Phys. Soc. Jpn.* **2012**, *81*, 034704.

(67) Bronger, W.; Ridder, G. Synthese und Struktur von $SrPdH_{2,7}$. *J. Alloys Compd.* **1994**, *210*, 53−55.

(68) Olofsson-MÅrtensson, M.; Kritikos, M.; Noréus, D. A Novel Tetrahedral Formally Zerovalent-Palladium Hydrido Complex Stabilized by Divalent Alkaline Earth Counterions. *J. Am. Chem. Soc.* **1999**, *121*, 10908−10912.

(69) Kohlmann, H.; Fischer, H. E.; Yvon, K. Europium Palladium Hydrides. *Inorg. Chem.* **2001**, *40*, 2608−2613.

(70) Götze, A.; Möllmer, J.; Kohlmann, H. From the Laves Phase $CaRh_2$ to the Perovskite $CaRhH_3$ − in Situ Investigation of Hydrogenation Intermediates $CaRh_2H_x$. *Inorg. Chem.* **2018**, *57*, 10925−10934.

(71) Van Mal, H. H.; Buschow, K. H. J.; Miedema, A. R. Hydrogen Absorption in $LaNi_5$ and Related Compounds: Experimental Observations and Their Explanation. *J. Less-Common Met.* **1974**, *35*, 65−76.

(72) Hemmes, H.; Driessen, A.; Griessen, R. Thermodynamic Properties of Hydrogen at Pressures up to 1 Mbar and Temperatures between 100 and 1000K. *J. Phys. C: Solid State Phys.* **1986**, *19*, 3571−3585.

(73) Driessen, A.; Sanger, P.; Hemmes, H.; Griessen, R. Metal Hydride Formation at Pressures up to 1 Mbar. *J. Phys.: Condens. Matter* **1990**, *2*, 9797−9814.

(74) Bronger, W.; Müller, P.; Schmitz, D.; Spittank, H. Synthese und Struktur von Na_2PtH_4, einem ternären Hydrid mit quadratisch planaren PtH_4^{2-}-Baugruppen. *Z. Anorg. Allg. Chem.* **1984**, *516*, 35−41.

(75) Ikeda, K.; Kato, S.; Ohoyama, K.; Nakamori, Y.; Takeshita, H. T.; Orimo, S. Formation of Perovskite-Type Hydrides and Thermal Desorption Processes in Ca−*T*−H (*T*=3d Transition Metals). *Scr. Mater.* **2006**, *55*, 827−830.

(76) Takagi, S.; Saitoh, H.; Endo, N.; Sato, R.; Ikeshoji, T.; Matsuo, M.; Miwa, K.; Aoki, K.; Orimo, S. Density-Functional Study of Perovskite-Type Hydride $LiNiH_3$ and Its Synthesis: Mechanism for Formation of Metallic Perovskite. *Phys. Rev. B* **2013**, *87*, 125134.

(77) Gencer, A.; Surucu, G. Investigation of Structural, Electronic and Lattice Dynamical Properties of $XNiH_3$ (X = Li, Na and K) Perovskite Type Hydrides and Their Hydrogen Storage Applications. *Int. J. Hydrogen Energy* **2019**, *44*, 15173−15182.

(78) Shannon, R. D. Revised Effective Ionic Radii and Systematic Studies of Interatomic Distances in Halides and Chalcogenides. *Acta Crystallogr., Sect. A: Found. Adv.* **1976**, *32*, 751−767.

(79) Bronger, W.; Jansen, K.; Breil, L. $Ca_2RhD_{5.4}$− Strukturbestimmung über Neutronenbeugungsexperimente. *Z. Anorg. Allg. Chem.* **1998**, *624*, 1477−1480.

(80) Bronger, W.; Breil, L. Calcium-Rhodium-Hydride – Synthese und Struktur. *Z. Anorg. Allg. Chem.* **1998**, *624*, 1819−1822.

(81) Orgaz, E.; Mazel, V.; Gupta, M. Electronic Structure and Electron-Phonon Coupling in Stoichiometric and Defective Hydrides $MPdH_3$ (*M*=Ca, Sr, Eu, Yb). *Phys. Rev. B* **1996**, *54*, 16124−16130.